EUROFUSION WP15ER-PR(16) 14856

A. Colaitis et al.

Crossed Beam Energy Transfer (CBET): assessment of the Paraxial Complex Geometrical Optics approach versus a time-dependent paraxial to describe experimental results

Preprint of Paper to be submitted for publication in
Physics of Plasmas

This work has been carried out within the framework of the EUROfusion Consortium and has received funding from the Euratom research and training programme 2014-2018 under grant agreement No 633053. The views and opinions expressed herein do not necessarily reflect those of the European Commission.

Crossed Beam Energy Transfer: assessment of the Paraxial Complex Geometrical Optics approach versus a time-dependent paraxial method to describe experimental results

A. Colaïtis,[1] S. Hüller,[2] D. Pesme,[2] G. Duchateau,[1] and V. T. Tikhonchuk[1]
[1)] *Université de Bordeaux - CNRS - CEA, Centre Lasers Intenses et Applications, UMR 5107, 351 Cours de la Libération, 33400 Talence, France*
[2)] *Centre de Physique Théorique, Ecole Polytechnique, CNRS, Université Paris-Saclay, 91128 Palaiseau, France*

(Dated: January 7, 2016)

The Crossed Beam Energy Transfer (CBET) of two large laser beams is modeled using two approaches: (i) based on time-independent Paraxial Complex Geometrical Optics (PCGO) for stochastically distributed Gaussian-shaped beamlets, and (ii) based on time-dependent conventional paraxial propagation of smoothed laser beams. Each description of the laser beam propagation is coupled to an hydrodynamics code. Both approaches are compared in a well-defined plasma configuration, with density- and velocity- profiles corresponding to an inhomogeneous plasma, including a resonance zone in which the matching conditions for a resonant coupling between the two laser beams are fulfilled. The comparison is made either for laser beams smoothed by a random phase plate (RPP) or for 'regular beams' without laser speckles and of the same size. In general, a very good agreement is found between the PCGO simulations and the fully time-dependent paraxial-type simulations carried out with the code Harmony. The role of the laser speckles in the case of smoothed laser beams is also investigated for each approach. The comparison shows that the code based on the PCGO approach correctly describes the CBET in situations where a resonant energy exchange occurs, past a transient period on the picosecond time scale. The PCGO-based CBET model is applied to the hydrodynamic simulation of a CBET experiment. The results are in overall good agreement with the experimental data. The conclusions presented in this paper are promising for the numerical modeling of the laser beams propagation in a complex geometry and for large cm-size plasma volumes.

I. INTRODUCTION

Laser-Plasma Interaction (LPI) is subject to numerous nonlinear couplings between the electromagnetic (EM) and the plasma waves[1–3]. Among these couplings, the overlap of several laser waves in the plasma produces ponderomotive beatings able to drive Ion Acoustic Waves (IAWs), and the latter can lead to an energy exchange between the incident laser waves. This process of Stimulated Brillouin Scattering (SBS), also referred to as Cross-Beam Energy Transfer (CBET), is notably important in Inertial Confinement Fusion (ICF). Early theoretical work[4] showed that resonantly excited IAWs can be driven in the baseline National Ignition Facility (NIF)[5] configuration, and CBET is now used to tune the symmetry irradiation in the ICF indirect drive on the NIF[6]. Direct-drive configurations have also been found to be subject to the CBET instability[7,8], affecting both the symmetry of implosion and the laser-target coupling. The processes at play in the CBET occur on a wide range of spatial and temporal scales. Typical plasmas in the ICF-related experiments have millimeter length scales and evolve on the nanosecond time scale. They are studied by means of radiative hydrodynamic codes. Thus, an efficient modeling of the CBET must be added to the hydrodynamic codes in order to design LPI experiments and to improve our understanding of the laser-plasma coupling,

The laser-plasma interaction in ICF hydrodynamic codes used for the design and the interpretation of ablation and implosion experiments rely on Ray-Tracing models (RT)[9]. The propagation and interaction of laser beams in plasma are modeled by bundles of needle-like rays characterized by a power density and following the geometrical optics (GO) laws and characterized by a power. The RT models are rather well suited to compute the inverse Bremsstrahlung energy deposition, but the modeling of the nonlinear laser-plasma interaction requires the knowledge of quantities such as the intensity and the direction of propagation of the laser beams, which are not available in standard RT packages. Inline models of CBET in Ray-Tracing based hydro-codes have been successfully implemented[7,8,10], although they require particular numerical methods and parameters, such as sub-time step iterations, local mesh refinement, CBET gain limitation, IAW amplitude limitation, and beam intensity renormalization to conserve energy. These difficulties arise from the fact that the laser beam intensity, direction and width are merely estimated on the basis of the inverse Bremsstrahlung absorption predicted by the Geometrical Optics (GO) rays. These difficulties are then essentially due to the errors on the computed laser intensities near the caustics, the loss of accuracy in the low density regions, and the dependence of the results with regards to the Lagrangian hydrodynamic mesh resolution, the topology of the latter depending on the plasma flows and not on the laser field gradients.

The ray-based Paraxial Complex Geometrical Optics (PCGO)[11] (see[12] for a review) is an alternate method

for describing scalar wave fields. This method has been adapted to the propagation of laser beams in collisional plasmas and implemented in the radiative hydrodynamic code CHIC[13,14]. The optically smoothed laser beams used in ICF, generated via phase plates and characterized by speckle patterns, can indeed be modeled by PCGO beamlets[15] so as to reproduce the relevant laser beam speckle intensity statistics. For clarity, we underline here the semantic distinction made in this paper: (i) the "laser beams" refer to the whole large laser beams, of which we compute the space-time evolutions, and (ii) the so-called "beamlets" are the elementary PCGO sub-elements used to compute the evolution of the laser beams; these beamlets are characterized by a Gaussian transverse intensity profile. The width and curvature radius of these beamlets depend on the plasma density gradients, and the PCGO method describes their propagation, refraction and diffraction.

In comparison with other methods to model a laser beam propagation, the ray-based Paraxial Complex Geometrical Optics greatly simplifies the numerical efforts to describe the Cross Beam Energy Transfer, because the key quantities for the computation of the steady-state power transfer[16] are readily known. Each intersection between pairs of beamlets is treated as a steady-state CBET occurring in a localized zone of plasma, with well-defined parameters interpolated at the coordinate of the beamlets centroids intersection. In this framework, the power transfer between the Gaussian beamlets can be determined either analytically or, at least, by means of a rapidly converging numerical integration over a limited zone[15,16]. Each laser beam is modeled by a great number of beamlets (typically less or equal to the number of speckles in the cross section of the beam) so that numerous beamlet-to-beamlet intersections reproduce the Cross Beam Energy Transfer between the large laser beams. This approach can be considered to be a method of discretization in space of the large domain where the laser beams interact between themselves, thus accounting for the spatial variation of plasma parameters in the interaction region. This model is implemented inline and without sub-timestep iterations. It takes into account the plasma inhomogeneity and is implemented in a way such that energy is naturally conserved.

Although being of great interest for the modeling of ICF implosions with realistic laser beams[15], the comparison of the numerical results for modeling CBET either with a time-resolved full scale paraxial electromagnetic code or with a code based on PCGO was still lacking to benchmark the validity of the latter approach.

We present in the present paper a study of the widespread CBET configuration in which the energy transfer takes place between two large laser beams interacting in a homogeneous or an inhomogeneous plasma. In order to check the validity and the accuracy of the PCGO method to model CBET, we carry out comparisons between the numerical results obtained with this method, with the results provided by the paraxial electromagnetic code HARMONY[17–19]. In the latter, the laser plasma coupling is based on time-dependent paraxial wave solvers for the electromagnetic waves embedded in a nonlinear hydrodynamics code describing together the plasma expansion and the plasma waves on the acoustic time scale.

The inhomogeneous plasma considered in the present article corresponds to configurations which can be found in indirect- and in direct-drive ICF schemes, in which the dependence of the plasma flow velocity with regards to the spatial coordinates is predominantly linear. Since the three-wave resonance conditions for Stimulated Brillouin Scattering (SBS) are only weakly affected by the density variations, the frequency mismatch in these SBS resonance conditions is essentially due to the inhomogeneity of the plasma flow.

The paper is organized as follows: in Sec. II, we present the analytical framework to model the resonant laser flux exchange associated with a SBS gain in an inhomogeneous plasma. Two cases are considered: (i) where the average intensity of the first laser beam (a pump) is many times greater than the average intensity of the second beam, and (ii) where both beams enter the interaction region with similar average intensities. The definitions of the interaction regimes and of the corresponding spatial gains in the cases of homogeneous and of inhomogeneous plasmas are essential for the understanding of the energy transfer between the beams. These various notions are presented in Sec. III. In Sec. IV, we study the energy transfer between two crossing beams; we present the comparison between the results of the simulations carried out with the PCGO method, with the simulations results obtained with the code HARMONY in two spatial dimensions (2D). The configurations studied in this section IV are essentially similar to the configurations presented in Sec. II. However, in addition to these configurations, we also study the case of laser beams with and without speckles patterns. In Sec. V, we finally compare our numerical data and their interpretation to the results of a reference experiment carried out on the NOVA laser facility[20] .

II. STEADY-STATE FORMULATION OF CBET IN AN EXPANDING PLASMA

A. General framework

We consider the energy transfer between two electromagnetic (EM) waves propagating in a plasma. The waves exchange energy through their scattering on the electron density perturbations of the ion acoustic wave (IAW) excited by the two EM waves crossing. This energy exchange is the most efficient in the resonant case when the beat frequency $\omega_{\rm beat} \equiv \omega_1 - \omega_2$ of the two laser waves is equal to the local IAW frequency, denoted as $\omega_{\rm IAW}$, of the ion acoustic wave of wave-vector $\mathbf{k}_s = \mathbf{k}_{\rm beat} \equiv \mathbf{k}_1 - \mathbf{k}_2$, $\mathbf{k}_1$ and $\mathbf{k}_2$ denoting the wavenumbers of the incident laser waves 1 and 2. This mech-

anism corresponds to the process of Stimulated Brillouin Scattering: the two EM waves, intersect each other at an angle denoted as θ, exciting the IAW with the wave vector $\mathbf{k}_s$. The frequency of this IAW is given, in the expanding plasma, by $\omega_{\rm IAW}(\mathbf{k}_s) = \omega_s + \mathbf{k}_s.\mathbf{V}_p$, where $\omega_s = \omega_s(\mathbf{k}_s)$ denotes the frequency, in a non-moving plasma, of the IAW with wave-number $\mathbf{k}_s$; $\omega_s(\mathbf{k}_s)$ is a function of k_s only, namely $\omega_s(\mathbf{k}_s) = \omega_s(k_s)$ with $k_s \equiv |\mathbf{k}_s|$. ω_s is given by $\omega_s^2 \equiv k_s^2 C_s^2$, with $C_s^2 \equiv [C_{se}^2/(1+k_s^2\lambda_{De}^2)] + 3v_{thi}^2$,$\lambda_{De}$ denoting the electron Debye length. $C_{\rm se}$ denotes the quantity $C_{\rm se} \equiv (ZT_e/m_i)^{1/2}$ with the usual notations for which Z, m_i and T_e denote the ion charge number, the ion mass, and the electron temperature, respectively; v_{thi} denotes the ion thermal velocity $v_{thi} \equiv (T_i/m_i)^{1/2}$, T_i being the ion temperature. The beating of the two laser waves is resonant with the IAW of wave-number $\mathbf{k}_s$ if the resonance condition $\omega_{\rm beat} = \omega_{\rm IAW}(k_s)$ is satisfied, i.e. if the condition $\omega_1 - \omega_2 = \omega_s(k_s) + \mathbf{k}_s.\mathbf{V}_p$ is fulfilled. It is consequently convenient to introduce the quantity

$$\delta\omega_{\rm mis} \equiv \omega_1 - \omega_2 - \mathbf{k}_s.\mathbf{V}_p - \omega_s(k_s)$$

so that the resonance condition reads $\delta\omega_{\rm mis} = 0$. In the particular case of equal laser frequencies, $\omega_1 = \omega_2$, the resonance condition becomes simply $\omega_s(k_s) = -\mathbf{k}_s.\mathbf{V}_p$.

Without any loss of generality, we may assume the following inequality $\omega_1 - \mathbf{k}_1.\mathbf{V}_p > \omega_2 - \mathbf{k}_2.\mathbf{V}_p$, so that the wave labeled as 1 will henceforth be referred to as the *pump* beam. The wave 2 will then be referred to as the *probe* beam.

With these notations, the coupled equations describing the evolution of the waves amplitudes in the slowly-varying envelope approximation read[21]:

$$(\partial_t + \nu_1 + \mathbf{V}_{g1}.\nabla)a_1 = -i\frac{\omega_{pe}^2}{2\omega_1}\left(\frac{\delta n}{n}\right)a_2 \ , \qquad (1)$$

$$(\partial_t + \nu_2 + \mathbf{V}_{g2}.\nabla)a_2 = -i\frac{\omega_{pe}^2}{2\omega_2}\left(\frac{\delta n^*}{n}\right)a_1 \ . \qquad (2)$$

The electric fields E_{w1} and E_{w2} of the waves 1 and 2 have been decomposed as $E_{w1} = E_1 \exp -i(\omega_1 t - \mathbf{k_1}.\mathbf{x}) + C.C.$ and $E_{w2} = E_2 \exp -i(\omega_1 t - \mathbf{k_2}.\mathbf{x}) + C.C.$. $\mathbf{V}_{gi} = c^2\mathbf{k_i}/\omega_i$ and ν_i denote the group velocity and the damping rate of wave i, respectively; the quantities a_i are the normalized electric field amplitudes $a_i \equiv v_{osci}/v_{the}$ with $v_{osci} \equiv q_e E_i/(m_e\omega_i)$, for $i = 1, 2$, v_{the} denoting the electron thermal velocity.

The ponderomotive force due to the two laser waves induce a low frequency density modulation, denoted as δn_s, which can be decomposed as $\delta n_s = \delta n \exp -i(\omega_{\rm beat} t - \mathbf{k_s}.\mathbf{x}) + C.C.$, so that δn is the component of the density modification which is at the frequency $\omega_{\rm beat} = \omega_1 - \omega_2$ and wave-number $\mathbf{k_s}$.

The linearized ponderomotive modification of the plasma density due to the beating of the two laser waves can be easily computed by Fourier transforming the linearized fluid equations and by imposing $\omega = \omega_{\rm beat} - \mathbf{k}_s.\mathbf{V}_p$, and $\mathbf{k} = \mathbf{k}_s$, where ω and $\mathbf{k}$ denote the Fourier variables. By doing so, and by including the IAW damping rate ν_s, one obtains the following relation

$$\left[(\omega_{\rm beat} - \mathbf{k}_s.\mathbf{V}_p)^2 + 2i\omega_s\nu_s - \omega_s^2\right]\left(\frac{\delta n}{n}\right) = S_{k_s},$$

with

$$S_{k_s} = \Gamma_s a_1 a_2^* \equiv \frac{k_s^2 C_{se}^2}{(1+k_s^2\lambda_D^2)^2} a_1 a_2^*,$$

n denoting the local plasma density, Γ_s is a convenient notation for the quantity $\Gamma_s \equiv k_s^2 C_{\rm se}^2/(1+k_s^2\lambda_{De}^2)^2$. Inserting the expression of $\delta n/n$ in the set of equations (2), one obtains

$$\begin{aligned}(\partial_t + 2\nu_1 + \mathbf{V}_{g1}.\nabla)|a_1|^2 &= +\frac{\omega_{pe}^2}{\omega_1}\Gamma_s \Im\left(\frac{1}{\mathscr{D}_s}\right)|a_1|^2|a_2|^2 \ , \\ (\partial_t + 2\nu_2 + \mathbf{V}_{g2}.\nabla)|a_2|^2 &= -\frac{\omega_{pe}^2}{\omega_2}\Gamma_s \Im\left(\frac{1}{\mathscr{D}_s}\right)|a_1|^2|a_2|^2 \ ,\end{aligned} \qquad (3)$$

with $\Im(1/\mathscr{D}_s)$ standing for the imaginary part of $1/\mathscr{D}_s$, where the function $\mathscr{D}_s = (\omega_{\rm beat} - \mathbf{k}_s.\mathbf{V}_p)^2 + 2i\omega_s\nu_s - \omega_s^2$ appearing in the denominator quantifies the resonance between the laser waves beating and the ion acoustic wave. In the following, for simplicity, we will restrict ourselves to the s-polarization for the EM waves, so that the vectors of the electric fields associated with a_1 and a_2 are both perpendicular to the plane defined by the vectors $\{\mathbf{k}_1,\mathbf{k}_2\}$.

At this stage it is interesting to make contact with the Stimulated Brillouin Scattering (SBS) instability in the regime of strongly damped IAW. We first introduce a new coordinate system along the respective wave propagation directions ξ and η with $\mathbf{k_1} = k_1\mathbf{e}_\xi$ and $\mathbf{k_2} = k_2\mathbf{e}_\eta$, as illustrated in Fig. 1. The unit vectors $\mathbf{e}_\xi$ and $\mathbf{e}_\eta$ are separated by the angle θ so that the coordinate system is generally non-orthogonal (except for $\theta = \pi/2$). We

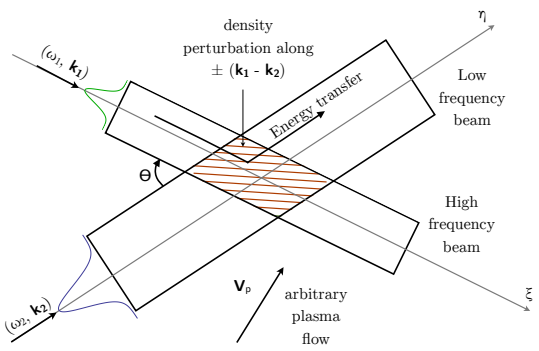

Figure 1. Schematic representation of the Cross Beam Energy Transfer configuration such as considered in the article. The higher frequency beam 1 propagates along the ξ axis and the lower frequency beam 2 along the η axis. The plasma parameters, density, temperature, velocity, are *a priori* arbitrary in the interaction region.

then normalize the intensities $|a_i|^2$ to the pump wave entrance intensity by setting $|a_i|^2 = \langle |a_1|^2_{\rm in}\rangle\ I_i$, in which $\langle |a_1|^2_{\rm in}\rangle$ denotes the average intensity value of the pump beam 1 taken at the *left hand side* entry (with respect to the coordinate η) of the interaction region.

The value of the pump beam (wave 1) normalized input intensity $\langle |a_1|^2_{\rm in}\rangle$ at its entrance in the domain of the interaction region reads

$$\langle |a_1|^2_{\rm in}\rangle = \frac{\langle v^2_{{\rm osc},1}\rangle}{v^2_{T,e}} = \frac{9.34\times 10^{-3}}{N_1 T_{e,{\rm keV}}}\frac{I_1\lambda_1^2}{10^{14}{\rm W}\mu{\rm m}^2/{\rm cm}^2}\ , \qquad (4)$$

where $N_1 = (1-\omega_p^2/\omega_1^2)^{1/2}$ denotes the plasma refractive index seen by wave 1, the latter being characterized by its vacuum wave length $\lambda_1 = 2\pi c/\omega_1$. Assuming a small difference between the frequencies ω_1 and ω_2 in the expression of the coupling coefficients, namely $\omega_1 - \omega_2 \ll \omega_1, \omega_2$, so that ω_2 can be replaced by ω_1, the equations (5) take the following form

$$\begin{aligned}(\partial_t + 2\nu_1 + V_{g1}\partial_\xi)\mathcal{I}_1 &= -2(\gamma_0^2/\nu_s)\ \mathcal{R}\ \mathcal{I}_1\mathcal{I}_2\ ,\\ (\partial_t + 2\nu_2 + V_{g2}\partial_\eta)\mathcal{I}_2 &= +2(\gamma_0^2/\nu_s)\ \mathcal{R}\ \mathcal{I}_1\mathcal{I}_2\ ,\end{aligned} \qquad (5)$$

where the resonance function $\mathcal{R}$ is given by the expression $\mathcal{R} \equiv 4\nu_s^2\omega_s^2/[(\Omega^2_{\rm beat} - \omega_s^2)^2 + 4\nu_s^2\omega_s^2]$, so that $\mathcal{R} = 1$ at the resonance $\Omega_{\rm beat} = \omega_s$. We introduced in this expression the symbol $\Omega_{\rm beat}$ defined by the relation $\Omega_{\rm beat} \equiv \omega_{\rm beat} - \mathbf{k}_s.\mathbf{V}_p$, and γ_0 denotes the SBS growth rate, with

$$\gamma_0^2 \equiv (\frac{n}{n_c})\frac{\omega_1}{4\omega_s}\frac{k_s^2 C_{\rm se}^2}{(1+k_s^2\lambda_{De}^2)^2}\langle |a_1|^2_{\rm in}\rangle\ ,$$

in which the frequency ω_s is itself a function of $k_s\lambda_{De}$, namely $\omega_s = k_s C_{\rm se}/(1+k_s^2\lambda_{De}^2)^{1/2}$.

In the steady-state limit, the previous equations (5) can be additionally simplified in the cases where the transverse EM damping rates ν_i are negligible and in the limit $V_{g2} = V_{g1}$. In these limits, the resulting system of equations, extensively studied in Ref. 22 for the case of a homogeneous plasma, takes the following form

$$\begin{aligned}\partial_\xi \mathcal{I}_1 &= -2\beta(\xi,\eta)\ \mathcal{I}_1\mathcal{I}_2\ ,\\ \partial_\eta \mathcal{I}_2 &= +2\beta(\xi,\eta)\mathcal{I}_1\mathcal{I}_2\ .\end{aligned} \qquad (6)$$

The quantities involved in the coupling coefficient $\beta(\xi,\eta) \equiv [\gamma_0^2/(\nu_s V_{g2})]\ \mathcal{R}$ are functions of the local plasma parameters $\{T_e, n_e, \mathbf{V}_p\}$ inside the interaction region, so that in general the coupling constant β is a function of the spatial coordinates (ξ,η).

B. Case of an expanding plasma

We now consider the energy exchange between two EM waves propagating in a plasma with a linear velocity profile, a constant density and a constant temperature. In the vicinity of the resonance point where $\Omega_{\rm beat} \approx \omega_s$, the resonance denominator $\mathscr{D}_s$ can be approximated by:

$$\mathscr{D}_s \approx 2\omega_s(\Omega_{\rm beat} - \omega_s + i\nu_s)\ . \qquad (7)$$

In this limit, the nonlinear coupling coefficient $\beta(\xi,\eta)$ becomes simply:

$$\beta(\xi,\eta) = \frac{\gamma_0^2/(\nu_s V_{g,2})}{1+\left[\frac{\Omega_{\rm beat}-\omega_s}{\nu_s}\right]^2}\ . \qquad (8)$$

In this expression of $\beta(\xi,\eta)$, the quantity $\Omega_{\rm beat} = \omega_{\rm beat} - \mathbf{k}_s.\mathbf{V}_p$ depends on space through the spatial dependence of $\mathbf{V}_p$. Let us first define the coordinate system to describe $\mathbf{V}_p$. We consider a generic point M and denote by O the point corresponding to the intersection of the central axis of beam 1 with the central axis of beam 2 (see Fig. 2). Concerning the Cartesian coordinates, we choose the y-axis to be the axis parallel to the expansion velocity $\mathbf{V}_p(y)$ and going through the point 0; the x-axis is the axis orthogonal to $\mathbf{V}_p(y)$ and going through the point 0. A generic point M will therefore be defined by its Cartesian coordinates (x,y), with $\mathbf{OM} = x\mathbf{e}_x + y\mathbf{e}_y$, $\mathbf{e}_x$ and $\mathbf{e}_y$ denoting the unit vectors of the axis Ox and Oy. We consider a plasma with a linear velocity profile of the form $\mathbf{V}_p(y) = [V_{p,0} + y\ c_s/L_\perp]\mathbf{e}_y$ for a point M of coordinates (x,y). Thus, $V_{p,0}$ is the plasma velocity at the point O of intersection of the axis of beam 1 and beam 2, and $L_\perp$ is the velocity gradient defined as: $L_\perp = c_s/(\partial_y V_p)|_{y=0}$ in this Cartesian coordinate system. We now denote by $\mathbf{e}_\eta$ and $\mathbf{e}_\xi$ the unit vectors along the axis $O\eta$ and $O\xi$ (see Fig. 2). In the coordinate system $(\mathbf{e}_\eta, \mathbf{e}_\xi)$, the vector $\mathbf{OM}$ is written as $\mathbf{OM} = \eta\mathbf{e}_\eta + \xi\mathbf{e}_\xi$ in which its coordinates η and ξ are given in terms of x and y through the relations

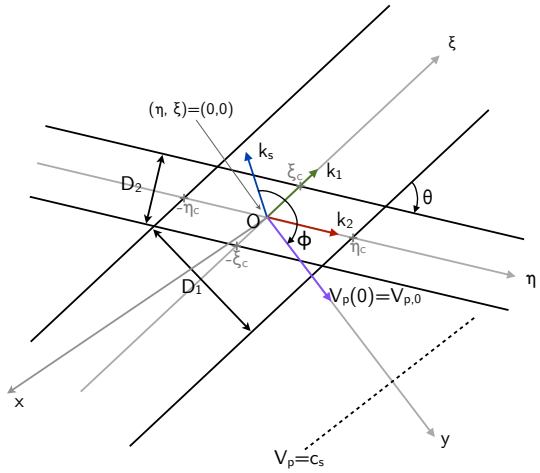

Figure 2. (color) Schematic representation of the CBET configuration. The high frequency beam 1 propagates along the ξ axis and the low frequency beam 2 along the η axis. The plasma flow velocity is in the s direction with value $V_{p,0}$ at the intersection between the beams centroids. The line of constant $V_p = c_s$ is indicated by a dashed line.

$x = \eta \mathbf{e}_x.\mathbf{e}_\eta + \xi \mathbf{e}_x.\mathbf{e}_\xi$ and $y = \eta \mathbf{e}_y.\mathbf{e}_\eta + \xi \mathbf{e}_y.\mathbf{e}_\xi$. Consequently, $\mathbf{V}_p(y) = [V_{p,0} + y\ c_s/L_\perp]\mathbf{e_y}$ becomes a function of η and ξ. We denote as ϕ the angle between $\mathbf{k}_s$ and $\mathbf{V}_p$, so that $\mathbf{e_y}.\mathbf{e}_\xi = -\sin(\phi+\theta/2)$ and $\mathbf{e}_y.\mathbf{e}_\eta = -\sin(\phi-\theta/2)$. In this coordinate system, $\beta(\xi,\eta)$ becomes

$$\beta(\xi,\eta) = \frac{\gamma_0^2/(\nu_s V_{g,2})}{1 + \frac{k_s^2 c_s^2}{\nu_s^2}\left[\mathcal{Q}_0 - \mathcal{Q}(\xi,\eta)\right]^2} \ , \tag{9}$$

with

$$\mathcal{Q}_0 = \frac{\omega_1 - \omega_2}{k_s c_s} - 1 \ ,$$
$$\mathcal{Q}(\xi,\eta) = \left| \frac{V_{p,0}}{c_s} - \frac{\eta \sin[\phi - (\theta/2)] + \xi \sin[\phi + (\theta/2)]}{L_\perp} \right| \cos\phi \ . \tag{10}$$

III. THEORETICAL GAINS AND COMPARISON WITH PCGO-BASED CBET

In the preceding section we have derived the equations that describe the coupling between two laser beams, together with the coupling coefficients relevant for an expanding plasma close to resonance. In this section these results will be used to determine the transfer from beam 1 (*pump* beam) to beam 2 (*probe* beam). To properly address the pump to probe transfer, taking into account the width of the laser beam, one has to integrate across the beam profiles.

Throughout this section, the amplification factor of beam 2, T_2, is defined as follows:

$$T_2 \equiv \int_{-\xi_c}^{\xi_c} \mathcal{I}_2^{\rm out}(\xi)\mathrm{d}\xi / \int_{-\xi_c}^{\xi_c} \mathcal{I}_2^{\rm in}(\xi)\mathrm{d}\xi \ , \tag{11}$$

In this expression, ξ_c is defined by $\xi_c \equiv \mathcal{D}_1/(2\sin\theta)$, $\mathcal{D}_1$ being the beam 1 diameter; the quantities $\mathcal{I}_2^{\rm out}$ and $\mathcal{I}_2^{\rm in}$ are given by $\mathcal{I}_2^{\rm out}(\xi) = \mathcal{I}_2(\xi,\eta_c)$, $\mathcal{I}_2^{\rm in}(\xi) = \mathcal{I}_2(\xi,-\eta_c)$ with $\eta_c \equiv \mathcal{D}_2/(2\sin\theta)$, $\mathcal{D}_2$ being the beam 2 diameter. The linear gain G_2 corresponding to the beam 2 amplification factor T_2 is defined by $G_2 \equiv \ln(T_2)$.

1. Small probe-to-pump intensity ratio

The pump beam remains unaffected by the pump-probe energy transfer throughout the interaction region whenever the intensity ratio I_2/I_1 is small, i.e. $I_2 \ll I_1$. Assuming an initially constant transverse profile for the beams, i.e. $\mathcal{I}_1^{\rm in}(\xi) = \mathcal{I}_1^{\rm in}$ and $\mathcal{I}_2^{\rm in}(\eta) = \mathcal{I}_2^{\rm in}$, the equation (6) yields:

$$\mathcal{I}_2^{\rm out}(\xi) = \mathcal{I}_2^{\rm in} \exp \int_{-\eta_c}^{\eta_c} 2\beta(\xi,\eta')\mathrm{d}\eta' \ , \tag{12}$$

so that Eq. (11) for the T_2 transmission factor reads:

$$T_2^{I_2 \ll I_1} = \frac{1}{2\xi_c} \int_{-\xi_c}^{\xi_c} \exp\left[\int_{-\eta_c}^{\eta_c} 2\beta(\xi,\eta)\mathrm{d}\eta\right] \mathrm{d}\xi \ . \tag{13}$$

The analytical integration of β in this equation requires the splitting of the integral above into two separate subdomains to account for the absolute value of the velocity in Eq. (10). These domains are delimited by the line where the plasma velocity is zero; this line is defined by $\eta\sin(\phi - \theta/2) + \xi\sin(\phi + \theta/2) = L_\perp V_{p,0}/c_s$. The corresponding gain factor $G_2^{I_2\ll I_1} = \ln(T_2^{I_2\ll I_1})$ accounts for the local plasma parameters in the interaction region along the directions ξ and η. For a finite length interaction in an inhomogeneous medium, $G_2^{I_2\ll I_1}$ has an *a priori* upper bound $G_{\rm max}$ given by[21]

$$G_{\rm max} \equiv \frac{2\gamma_0^2 L_{\rm int}}{\nu_s V_{g,2}} \ , \tag{14}$$

so that one has $G_2^{I_2\ll I_1} \leq G_{\rm max}$. $L_{\rm int}$ denotes the maximum interaction length for a resonant coupling; $L_{\rm int}$ is given by the minimum between the interaction length in an inhomogeneous plasma, denoted as $L_{\rm inh}$, and the beam width, denoted as $L_{\rm beam}$, namely $L_{\rm int} \equiv \min\{L_{\rm beam}, L_{\rm inh}\}$; in these expressions $L_{\rm inh}$ is given by

$$L_{\rm inh} = \pi \frac{L_\perp \nu_s/\omega_s}{\cos\phi \sin[\phi - (\theta/2)]} \ , \tag{15}$$

and $L_{\rm beam}$ by

$$L_{\rm beam} = \frac{\mathcal{D}_1}{2\sin\theta} \ , \tag{16}$$

$L_{\rm int}$ reduces to $L_{\rm inh}$ in the case $L_{\rm inh} < L_{\rm beam}$ when the inhomogeneity is the limiting factor for the gain; $G_{\rm max}$ is then the so-called Rosenbluth gain[23], denoted as $G_{\rm Ros}$ for what concerns the intensity amplification and given by $G_{\rm Ros} = (2\pi\gamma_0^2/\omega_s V_{g,2}))L_{\perp,\rm eff}$, where $L_{\perp,\rm eff} = L_\perp/[\cos\phi\sin[\phi - (\theta/2)]]$ denotes the effective flow gradient length.

For the case discussed in this article, we have chosen the following reference parameters for the plasma: $\nu_s/\omega_s = 10^{-1}$, $n_e/n_c = 10^{-1}$, $T_e = 3$ keV, $Z = 2.5$, $ZT_e \gg T_i$, and the mass number $m_i/m_p = 4.252$, m_p being the proton mass. The beam parameters are the following: the intensity of beam 1 in vacuum, I_1, is given by $I_1\lambda_L^2 = 0.9 \times 10^{14}$ Wμm^2/cm^2, the intensity of beam 2 satisfies the condition $I_2 \ll I_1$; both beams have equal diameters $\mathcal{D}_1 = \mathcal{D}_2 = \mathcal{D} = 600\lambda$, they have equal wavelengths $\lambda = 351$ nm, and the angles between them is $\theta = 20°$.

The intensity profiles of beams 1 and 2 at their entrance in the interaction region, denoted as $\mathcal{J}_1$ and $\mathcal{J}_2$, are the following

$$\mathcal{J}_1(\eta) = \exp\left[-\left|\frac{\eta\sin\theta}{\mathcal{D}}\right|^8\right] \ ,$$
$$\mathcal{J}_2(\xi) = \mathcal{I}_{2:1}\exp\left[-\left|\frac{\xi\sin\theta}{\mathcal{D}}\right|^8\right] \ , \tag{17}$$

where $\mathcal{I}_{2:1}$ denotes the upstream beam 2/beam 1 intensity ratio. Such profiles can be easily produced by means

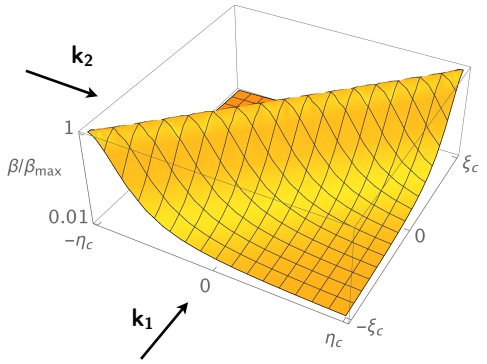

Figure 3. Illustration of the resonance function considered in this article, normalized to its maximum value. The two waves enter the domain along the upper-left and bottom-left boundaries of the domain, such as indicated by arrows. Note that the ξ and η axis are shown as if they were orthogonal, but actually one intersects the other with the acute angle $\theta = 20°$.

of Random Phase Plates. The beam widths can be considered to remain constant throughout the interaction region, in agreement with the assumptions made in Sec. II. The plasma velocity profile is linear, with $L_\perp = 500\lambda_L$, $V_{p,0} = c_s$ and $\phi = \pi$. The resulting resonance function is illustrated in Fig. 3. The corresponding theoretical gain $G_2^{I_2 \ll I_1}$ is computed by numerical integration of Eq. (11). We find a beam 2 intensity amplification $T_2^{I_2 \ll I_1} = 685$, so that the corresponding gain factor is $G_2^{I_2 \ll I_1} = 6.53$. By comparison, the value of $G_{\max}$ is $G_{\max} = 8.51$.

This theoretical configuration is reproduced with PCGO, modeling each super-Gaussian beam by $N_B = 100$ PCGO Gaussian beamlets in a planar two-dimensional geometry. The beamlets are pseudo-randomly focused around the interaction region so as to reproduce the intensity distribution of beams smoothed by Kinoform Phase Plates (KPP), as described in Ref. 15. The resulting intensity pattern is comparable to what would be obtained with a real speckle distribution, with larger speckles of radii $\sim 5 - 50\lambda_L$. This pseudo-speckle pattern produced with PCGO is able to model the correct intensity distribution in a plasma of laser beams smoothed by KPPs in the intensity domain between $0.1\langle I\rangle$ and $5\langle I\rangle$, where $\langle I\rangle$ denotes the mean laser intensity. The higher intensity statistics cannot be reproduced due to the limitations imposed by the minimum size of PCGO beamlets (see Refs. 15 and 24). The CBET gain $G_{\text{inh,PCGO}}^{I_2 \ll I_1}$ is computed as a discrete version of Eq. (11), where the summation spans over the beam 2 beamlets, namely

$$\exp G_{\text{inh,PCGO}}^{I_2 \ll I_1} = \frac{\sum_{k=1}^{N_B} I_k^{\text{out}} w_k^{\text{out}}}{\sum_{k=1}^{N_B} I_k^{\text{in}} w_k^{\text{out}}} , \qquad (18)$$

where I_k and w_k stand for the intensity and width of the beamlet k, respectively. The PCGO-based CBET model yields $T_{\text{PCGO}}^{\text{ros}} = 700$, corresponding to $G_{\text{inh,PCGO}}^{I_2 \ll I_1} = 6.55$. The simulation results are in excellent agreement with the theory in this case, and also for other values of $L_\perp$, θ, ϕ, n_e/n_c in the validity domain of the theory presented in Sec. II. The main constraint is the validity of Eq. (7), the latter limiting the range of $L_\perp$ which can be explored.

For two beams, modeled by $N_B = 100$ beamlets each one, the large-scale resonance function is discretized by 10^4 beamlet intersections. The energy transfer between the intersecting beamlets is computed by applying Eq. (6) to each intersection. Since the size of the beamlets is small compared to the overall beams, the coupling coefficient β from Eq. (8), being evaluated at the center of the intersection for the local plasma parameters, is assumed to be constant around the intersection centroid (defined as $(\eta, \xi) = (0, 0)$ for each). The accuracy of this method is naturally related to the width of each elementary beamlet intersection region compared to the width of the resonance function. In practice, the Gaussian beamlets used in PCGO are small compared to the characteristic inhomogeneities encountered in the typical CBET configurations. As an example, for a typical direct-drive ICF configuration, CBET occurs near the resonance region ($V_{p,0} = c_s$), where the gradient scale lengths of the density, temperature and velocity are much larger than the typical beamlet width of 10-30 λ_L. In configurations where this assumption would not be correct, the precision of the PCGO-based CBET model may be enhanced by replacing $\beta(0,0)$ by the average value of the nonlinear coupling coefficient in the interaction zone $\int\int \beta(\xi,\eta)\mathrm{d}\xi\mathrm{d}\eta/(4\xi_c\eta_c)$, for each elementary energy transfer between beamlets.

2. *Interaction between beams of similar intensities*

We now consider the case where the ratio of the beam intensities at their entrance in the crossing domain, $\mathcal{I}_{2:1} \equiv \mathcal{I}_2^{\text{in}}/\mathcal{I}_1^{\text{in}}$, is close to unity. In this regime the pump depletion has to be taken into account. For inhomogeneous plasmas, the estimate of the gain in such cases requires a direct numerical resolution of the equation (6). This numerical integration is the most efficiently achieved by taking the crossed derivatives in the equations (6):

$$\begin{aligned} \partial_\eta \partial_\xi \mathcal{I}_1 &= -2\partial_\eta (\ \beta(\xi,\eta)\ \mathcal{I}_1\ \mathcal{I}_2\ )\ , \\ \partial_\xi \partial_\eta \mathcal{I}_2 &= 2\partial_\xi (\ \beta(\xi,\eta)\ \mathcal{I}_1\ \mathcal{I}_2\ )\ . \end{aligned} \qquad (19)$$

This system is integrated using the Implicit Differential-Algebraic solver[25–27]. The initial conditions are defined on the input boundaries of the interaction region for both beams; there are consequently four initial conditions to specify; $\mathcal{I}_1(-\xi_c,\eta)$, $\mathcal{I}_1(\xi,-\eta_c)$, $\mathcal{I}_2(\xi,-\eta_c)$ and $\mathcal{I}_2(-\xi_c,\eta)$. Two of these are the initial intensity profiles of the beams, $\mathcal{J}_1(\eta) = \mathcal{I}_1(-\xi_c,\eta)$ and $\mathcal{J}_2 = \mathcal{I}_2(\xi,-\eta_c)$, defined by Eqs. (17).

The other two initial intensities, denoted $\mathcal{G}_1(\xi) = \mathcal{I}_1(\xi,-\eta_c)$ and $\mathcal{G}_2(\eta) = \mathcal{I}_2(-\xi_c,\eta)$, are solutions of the

partial differential equations (6) for the intersection region edges:

$$\partial_\xi \mathcal{G}_1(\xi) = -2\beta(\xi,-\eta_c)\ \mathcal{G}_1(\xi)\ \mathcal{J}_2(\xi)\ ,$$
$$\partial_\eta \mathcal{G}_2(\eta) = 2\beta(-\xi_c,\eta)\ \mathcal{G}_2(\eta)\ \mathcal{J}_1(\eta)\ , \qquad (20)$$

where the initial conditions for these equations are $\mathcal{G}_1(-\xi_c) = \mathcal{J}_2(-\xi_c) = \mathcal{I}_{2:1}\exp(-1)$ and $\mathcal{G}_2(-\eta_c) = \mathcal{J}_1(-\eta_c) = \exp(-1)$.

We integrate Eqs. (19) and (20) for two intensity ratios: $\mathcal{I}_{2:1} = 1$ and $\mathcal{I}_{2:1} = 1/8$. The other plasma and beam parameters are the same as in Sec. III 1. The theoretical gains computed from the probe beam power amplification are, for the two cases, $G_{\rm inh}^{1:8} = 2.061$ and $G_{\rm inh}^{1:1} = 0.692$. Simulations using the PCGO-based CBET model and the intensity profiles (17) yield the gain values $G_{\rm inh,PCGO}^{1:8} = 2.056$ and $G_{\rm inh,PCGO}^{1:1} = 0.692$, which are in excellent agreement with the theory. Furthermore, the output intensity profiles obtained with the numerical solution and the PCGO modeling are also in excellent agreement one with the other. Thus, the PCGO modeling is able to accurately reproduce the regions of pump depletion and probe beam amplification. This conclusion is discussed further in Sec. IV B 2 in the comparison of the PCGO results with the paraxial solver ones.

IV. CBET MODELING USING PARAXIAL ELECTROMAGNETIC WAVE SOLVERS

In order to describe the propagation of two well separated electromagnetic waves, paraxial wave solvers for the electric field (or the vector potential) of each beam are used. For the interaction of two electromagnetic waves, a system of partial differential equations using paraxial operators has to be solved with terms describing the coupling between the various modes[17–19]. Instead of the system of equations for the beam intensities (5), a system of equations for the corresponding complex-valued amplitudes is solved in the Cartesian coordinates. The main axis x is directed along the bisector of the propagation direction of the two interacting beams.

A. Formalism of the HARMONY code

The code HARMONY[17–19] has initially been designed to describe the coupling of two electromagnetic waves, with amplitudes a_+ and a_-, propagating in opposite directions. The coupling of these two waves is then mediated by short-wavelength IAWs.

In the configuration considered in the present article, the two laser beams propagate in the same direction, the angle θ between their axis satisfying the condition $\theta < 25°$, in which case the IAWs generated by their beating propagate perpendicularly to the symmetry axis located between the directions of propagation of the two crossing beams. To simplify, we will consider that the two incident transverse waves have the same frequency $\omega_1 = \omega_2$ that we will write as ω_t, and consequently the same damping coefficients $\nu_1 = \nu_2 = \nu_t$ and the same group velocity modulus, $V_{g,1} = V_{g,2} = V_{g,t}$. Therefore, in the code HARMONY, the counter-propagating field a_- is set to zero and the field a_+ contains two components

$$a_+ \equiv e^{i\mathbf{k}_\parallel\cdot\mathbf{x}}[a_1 e^{i\mathbf{k}_\perp\cdot\mathbf{y}} + a_2 e^{-i\mathbf{k}_\perp\cdot\mathbf{y}}]\ . \qquad (21)$$

In this decomposition, the wave vectors $\pm\mathbf{k}_\perp$ denote the wave vector components transverse to the symmetry axis Ox, namely $|\mathbf{k}_\perp| = |\mathbf{k}_1|\sin(\theta/2)$, with $|\mathbf{k}_1| \equiv k_1 = (N_1\omega_1/c)$. $\mathbf{k}_\parallel$ denotes the wave vector component along the symmetry axis, with $\mathbf{k}_\parallel = \mathbf{e}_x|\mathbf{k}_1|\cos(\theta/2)$. The equation for the field a_+ reads:

$$\mathcal{L}_{\rm par}(a_+) = -i\frac{\omega_1}{2}\frac{\delta n}{n_c}a_+ \qquad (22)$$

where $\delta n = (n - n_{\rm eq})$ is the density perturbation around the equilibrium density $n_{\rm eq}$ and where $\mathcal{L}_{\rm par}(a_+)$ is the paraxial operator $\mathcal{L}_{\rm par}(a_+) = [\partial_t + V_{gt,x}\partial_x + \nu_t - i(c^2/2\omega_t)\triangle_\perp]a_+$, with $V_{gt,x} \equiv V_{g,t}cos(\theta/2)$. The field a_+ is generated by considering two separate wave-fields for a_1 and a_2 in Fourier space, corresponding to their near field. Each wave-field is centered around $\pm\mathbf{k}_\perp$, respectively, with a width $\pm\Delta k$ that has to be smaller than $|\mathbf{k}_\perp|$. The wave-fields are smoothed by random phase plate (RPP) elements whose width δk is a fraction of $\Delta k \equiv k_1/[1 + 4f_\#^2]^{1/2}$ (see Ref. 28), with the focusing f-number $f_\# = 7$. The overall field a_+ has hence no on-axis field components and the initial fields a_1 and a_2 are spatially separated in y at $x = 0$, for $|\mathbf{k}_\perp|$ in the interval $|\mathbf{k}_\perp| < |\mathbf{k}_1\ [\sin(\theta/2) - 1/(2f_\#)]|$. The latter condition is fulfilled e.g. at $\theta = 20°$ for $f_\# > 3$.

The density perturbation entering in Eq. (22) is described by the hydrodynamic equations:

$$\partial_t n + \nabla n\mathbf{V} = 0\ , \qquad (23)$$
$$\partial_t\left(n\mathbf{V}\right) + \nabla\left(n\mathbf{V}\mathbf{V}\right) + C_s^2\nabla n + n\hat{\nu}_k\mathbf{V} = -nC_{\rm se}^2\nabla U_0\ ,$$

where $\hat{\nu}_k$ is a wavelength-dependent operator accounting for collisional damping and IAW Landau damping. The ponderomotive force acting on the plasma fluid following Eqs. (23), $\propto \nabla U_0$, takes into account the coupling between the components a_1 and a_2 of a_+, namely $(\nabla U_0)_{\rm CBET} \propto \nabla a_1 a_2^* \exp(i2|\mathbf{k}_1|y\sin\theta/2)$, and the square terms $(\nabla U_0)_{\rm self} \propto \nabla(|a_1|^2 + |a_2|^2)$, responsible for self-focusing.

B. Comparison between PCGO and HARMONY simulations

The steady-state CBET results obtained with the PCGO model are compared with the results obtained from the time-dependent paraxial code HARMONY in several cases corresponding to various probe to pump intensity ratios $\mathcal{I}_{2:1}$ and overlapped intensities $[I\lambda_L^2]^\Sigma$ (defined in free space), for beams of equal wavelength $\lambda_L = 1.05$

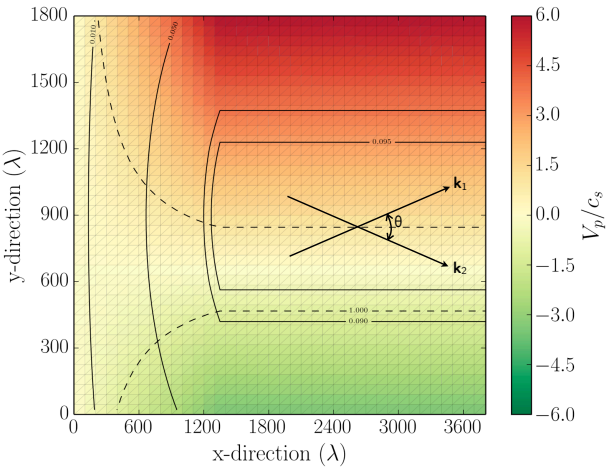

Figure 4. (color) Initial plasma parameters of the simulations. The color background indicates the plasma velocity $\mathbf{V}_p.\mathbf{e}_y$ in units of c_s. Negative values mean that the flow is directed along the unit vector $-\mathbf{e}_y$. The contours of constant density are shown in black plain lines, for $n_e/n_c \in \{0.01, 0.05, 0.09, 0.095\}$, and the contours of constant velocity are shown in black dashed lines for $\mathbf{V}_p.\mathbf{e}_y = \pm c_s$. In the domain $x < 1200\lambda_L$ the plasma density slowly increases as a function of x, so that the main interaction zone starts only from $x > 1200\lambda_L$.

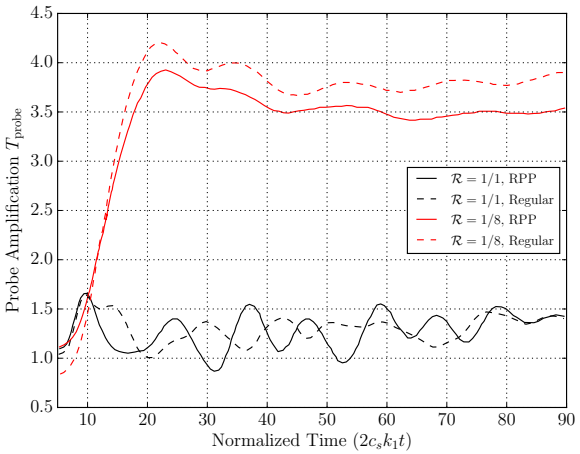

Figure 5. (color) Time history of the probe amplification T_2 from HARMONY simulations for a single realization of a RPP. The results at $[I\lambda_L^2]^\Sigma = 0.9\times10^{14}$ Wμm^2/cm^2 for $\mathcal{I}_{2:1} = 1/8$ and $\mathcal{I}_{2:1} = 1/1$ are indicated with red (grey) lines and black lines, respectively. The cases of RPP smoothed beams (i.e. with speckles) are shown with plain lines and the cases of 'regular' beams (i.e. without speckles) at the same average beam intensities are shown with dashed lines. The time is normalized to $(2k_1c_s)^{-1}$.

μm. The 2D simulation setup is a box of 4000 λ_L in length and 1800 λ_L in width in the (x, y) coordinate system. The velocity and density profiles mimic that of a thin-foil experiment, with a quadratic density profile and a linear expansion velocity. For $x \in [1300, 4000]\lambda_L$, the velocity is along the y direction and is described by

$$V_p(y)/c_s = (y - 657\lambda_L)/(200\lambda_L) \ , \qquad (24)$$

and the density is modeled by

$$n_e(y)/n_c = 0.0995 - [(y - 900\lambda_L)/(1580\lambda_L)]^2 \ , \qquad (25)$$

with $y \in [0, 1800]\lambda_L$. Note that the line of $V_p = 0$ does not correspond to the density maximum, as in a thin-foil experiment if only one side of the foil is irradiated by laser beams. These profiles are linearly extended, *via a ramp*, to zero velocity and zero density in the $x \in [0, 1300]\lambda_L$ interval in order to avoid spurious couplings of edge modes to plasma waves. The resulting initial plasma conditions are illustrated in Fig. 4

The plasma is fully ionized hydrogen, with $Z = 1$ and $m_i/m_p = 1$; the IAW damping rate is chosen to be $\nu_s/\omega_s = 1/10$. With these parameters, the plasma velocity at the center of the interaction region is $V_{p,0} = 1.2c_s$ in the direction of increasing y and the density is $n_e = n_c/10$. The position of the resonance can be obtained by equating $\mathcal{Q}(\eta, \xi)$ and $\mathcal{Q}_0$ in Eq. (10), which yields the optimal plasma velocity $V_{p,\rm opt} = \mathcal{Q}_0/\cos(\phi) = c_s$ at $y \approx 860\lambda_L$. The mean intensity profiles (envelop) of the beams are defined similarly to Eq. (17), with the exception of the normalizing factor:

$$\langle \mathcal{J}_1(\eta)\rangle = \frac{1}{1+\mathcal{I}_{2:1}} \exp\left[-\left|\frac{\eta\sin\theta}{\mathcal{D}}\right|^8\right] \ ,$$
$$\langle \mathcal{J}_2(\xi)\rangle = \frac{\mathcal{I}_{2:1}}{1+\mathcal{I}_{2:1}} \exp\left[-\left|\frac{\xi\sin\theta}{\mathcal{D}}\right|^8\right] \ , \qquad (26)$$

with $\mathcal{D} = 600\lambda_L$. The beams intersect in their focal plane in a region centered near the resonance line, at $x = 2650\lambda_L$ and $y = 900\lambda_L$. The beam crossing geometry in our simulations is simplified with respect to the general scheme presented in Fig. 2, since the plasma flow velocity is parallel to k_s (i.e. $\phi = 0$).

The comparison between the PGCO and the HARMONY results relies on two sets of observables. First, a systematic study of the asymptotic power transfer between the beams is made for various values of the beam intensity ratio $\mathcal{I}_{2:1} = \mathcal{I}_2^{\rm in}/\mathcal{I}_1^{\rm in}$, namely $\mathcal{I}_{2:1} = \{1,\ 1/8,\ 1/64\}$, measured in terms of $T_2 = \mathcal{P}_2^{\rm out}/\mathcal{P}_2^{\rm in} = \int \mathcal{I}_2^{\rm out} d\xi / \int \mathcal{I}_2^{\rm in} d\xi$, as a function of the interaction parameter $[I\lambda_L^2]^\Sigma$. Secondly, we study the various spatial patterns related to the CBET modeling, including: (i) the location and amplitude of the IAWs excited by the beams interaction, (ii) the intensity pattern of the beams in the simulation volume, and (iii) the deviation of the beams after the transfer region.

Two series of simulations with HARMONY and PCGO have been carried out using two types of beams, namely: (i) optically 'smoothed' beams generated by phase plates in the near field, thus producing a speckle pattern for

each beam in the interaction region (using Random Phase Plates (RPP) for HARMONY and Kinoform Phase Plates (KPP) for PCGO), and (ii) 'regular' beams of the same width and the same intensity envelope as the 'smoothed' beam, but without speckles. In both cases, the width in the interaction volume is controlled by applying a super-Gaussian envelope to the beams. The smoothed beam simulations describe realistic cases, while the regular beam simulations are carried out to assess the spatial patterns arising in the transfer region. The fractional power transfer in simulations with regular and smoothed beams are found to be comparable, as it can be seen in Fig. 5. The relaxation time observed in the simulations depend on the interaction parameters and the speckle pattern realization. It should be noted that each intensity pattern generated in simulations via RPP or KPP are single realizations and follow only partially the speckle intensity distribution known for the ensemble average[28–30]. The duration of the transient period, defined as the time it takes for the power transfer to reach its final value (either asymptotically or with small oscillations around a mean value), is in general in the order of $\sim 40-70$ in units of $(2c_s k_1)^{-1}$, corresponding to $\sim 7-12$ in units of $\omega_s^{-1} = (2c_s k_1 \sin\theta/2)^{-1}$, that is $t \sim 5{-}10$ ps at $\lambda_L = 0.35$ μm.

1. *Asymptotic power transfer*

The asymptotic power transfers obtained with both models are summarized in Fig. 6. For each value of the interaction parameter $[I\lambda_L^2]^\Sigma$, the results for both codes are determined from numerous simulations in which the random speckle pattern is varied via different phase plate realizations. The power transfer values are reliable around the average values (black points for HARMONY and green solid curve for PCGO) within the standard deviation (error bars and green shadows, respectively) on the basis of 16 realizations for each case (the convergence is observed to begin with at least 8 realizations). The results obtained with HARMONY are extracted from the averaged steady-state power transfer. The time-history of the ensemble-averaged power transfer (over the various simulations with various random speckle patterns) is illustrated in Fig. 7 for the $\mathcal{I}_{2:1} = 1/8$ case. As mentioned just above, the steady-state is reached for time scales of the order of 5 ps.

The PCGO and HARMONY codes produce results in good agreement one with the other, for a wide range of pump intensity values and for various pump/probe intensity ratios. The dispersion (standard deviation) of the results from HARMONY and PCGO-based CBET depend on the speckle size, on the first hand, and on the choice of the beamlet size, on the other hand. This dispersion can be characterized by the relative error ε, ε being defined as the ratio of the standard deviation to the probe amplification. The standard deviation for $f_\# = 7$ shows a relative error of the order of $\varepsilon \sim 12-13\%$ in

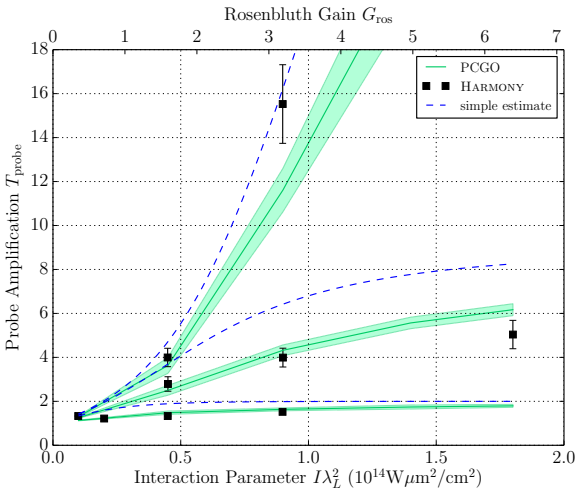

Figure 6. (color) Probe amplification as a function of the interaction parameter $[I\lambda_L^2]^\Sigma$ in units of 10^{14} Wμm^2/cm^2 for 3 values of the upstream intensity ratio $\mathcal{I}_{2:1}$ =1 (lower curves and points), 1/8 (center), and 1/64 (upper). The results obtained with the PCGO-based CBET model are shown with solid lines and the results from HARMONY with symbols. In both codes, each point for a given interaction parameter is based on 16 simulations using different random speckle patterns. The resulting ±1 standard deviation is shown as error bars for HARMONY and with a shaded envelope for PCGO. Estimated values from Eq. (27) are shown as blue dashed lines. The upper horizontal scale indicates the Rosenbluth gain values corresponding to the $I\lambda_L^2$ values of the bottom scale.

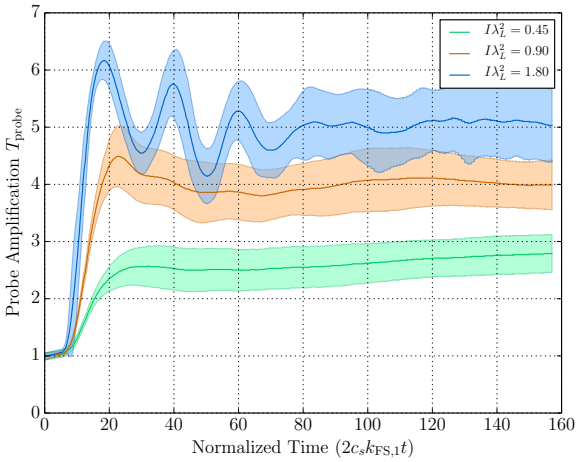

Figure 7. Time-history results from HARMONY: probe amplification in the $\mathcal{I}_{2:1} = 1/8$ case, exhibiting the statistical variance due to the different random speckle patterns. The solid lines represent the average value, while the corresponding shaded areas correspond to the ± 1 standard deviation region. The blue line and the blue-shaded area correspond to $[I\lambda_L^2]^\Sigma$ =1.8, the orange line and the orange-shaded area correspond to $[I\lambda_L^2]^\Sigma$ =0.9, and the green line and the green-shaded area correspond to $[I\lambda_L^2]^\Sigma = 0.45 \times 10^{14}$ Wμm^2/cm^2.

the HARMONY results, independently of the probe/pump ratio. For smaller speckles, corresponding to a smaller f-number, the relative error decreases due to the increased number of speckles in the crossing volume. For $f_\# = 5$ we find a relative error $\varepsilon \sim 8\%$. The influence of the high intensity speckles[30], not fitting well to the ensemble average, is evidently reduced for smaller speckle sizes (i. e. for smaller f-numbers). In the PCGO simulations, the relative error of the probe amplification (in its asymptotic value) depends more strongly on the number of beamlets chosen for the computation than on their size . The curves shown in Fig. 6 are based on 100 beamlets of width $10\lambda_L$ at their focal points, resulting in an error of $\varepsilon \sim 10\%$, approximately, slightly smaller than for the $f_\# = 7$ HARMONY simulations.

After accounting for the statistical fluctuations, both models are in quite good agreement one with the other, for intensities up to $[I\lambda_L^2]^\Sigma \leq 1.5 \times 10^{14}$ Wμm^2/cm^2. This is thought to be related to the splitting algorithm employed in PCGO: the overlap of PCGO beamlets does not reproduce the wings of the larger laser beam as much as in HARMONY. Consequently, the inverse transfer resonance region is less covered in the PCGO-based CBET simulations than in the HARMONY simulations, thus leading to an overestimate of the power transfer. Note that this limit is not an issue inherent to the PCGO model itself; it is due to its present formulation in the case of KPP smoothed beams (see Ref. 15).

Finally, it should also be noted that the HARMONY simulations at high intensities and for $\mathcal{I}_{2:1} = 1$ do not necessarily reach a steady-state regime: the power transfer may not converge to the single value seen in the PCGO simulations ($\mathcal{P}_2^{\rm out}/\mathcal{P}_2^{\rm in} \sim 1.66$), but rather oscillates between two values $1.1 < \mathcal{P}_2^{\rm out}/\mathcal{P}_2^{\rm in} < 1.4$. In this case, a mutual energy exchange takes place between the beams, due to the fact that the resonance zone corresponding the inverse energy transfer is not too far. HARMONY also takes into account the self-focusing (via the term $(\nabla U_0)_{\rm self}$, see Sec. IV A) of individual speckles, this effect depending on the speckle pattern realization. The discrepancy at high intensities can also be thought to be related to the modeling of the beam wings in the PCGO simulations.

Figure 6 also shows, in blue curves, estimates of the power transfer in terms of the probe amplification $T_{\rm probe}$ computed with the analytical model derived for a homogeneous plasma in Refs. 22, 31, and 32. It is given by

$$T_{\rm probe} = (\mathcal{I}_{2:1}\tilde{G})^{-1} \log\left[1 + e^G\left(e^{\mathcal{I}_{2:1}\tilde{G}} - 1\right)\right], \qquad (27)$$

where G is the gain value associated to the transfer, and $\tilde{G}$ the corresponding value defined by $\tilde{G} = G\mathcal{D}_1/\mathcal{D}_2 = G\xi_c/\eta_c$, see section III 1. For an inhomogeneous plasma, such in the cases discussed here, under the condition that the resonant zone is well confined inside the zone of the beams overlapping, one can take for G the Rosenbluth gain $G_{\rm Ros}$ given by Eq. (15) as a good approximation. For simplicity, we have taken the same value for $\tilde{G}$, namely $\tilde{G} = G_{\rm ros}$. In this case, the probe amplification $T_{\rm probe}$ has a small gain behavior of the form $T_{\rm probe} \to 1+G$ for $G = \tilde{G} \ll 1$, and a saturation behavior such as $T_{\rm probe} \to 1 + 1/\mathcal{I}_{2:1}$ for a large gain $G = \tilde{G} \gg 1$. This simple model shows a qualitative agreement with the simulations, although it overestimates (by a factor up to 2) the power transfer in the intermediate regime (G neither small nor large) at least for not too small $\mathcal{I}_{2:1}$ values. This model can still be kept as a rough guideline for the power transfer for angles up to $\theta < 45°$, as does the model from Refs. 33 and 34 for almost oppositely crossed beams[35].

2. Spatial characterization

As mentioned before, two resonance lines are present in the interaction region, defined here by $\mathbf{V}_p.\mathbf{e}_y = \pm c_s$. The asymptotic value of the energy transferred between the beams depends on the balance between the power transfer from the downward beam to the upward beam in the region where $\mathbf{V}_p.\mathbf{e}_y > 0$, and the power transfer from the upward beam to the downward beam in the region where $\mathbf{V}_p.\mathbf{e}_y < 0$. Given the input velocity profiles, these lines are located at $y_{c_s,+} = 860\lambda_L$ and $y_{c_s,-} = 460\lambda_L$. These two locations are expected to be the domains of maximum IAW amplitude. The relative density perturbation $\delta n/n_{\rm eq}$ ($n_{\rm eq}$ denoting the unperturbed density) is obtained in HARMONY from the resolution of the nonlinear fluid equations (23). In the PCGO-based CBET model, this amplitude can be estimated in the framework presented in Sec. II by writing the equation for the evolution of the ion density perturbation,

$$[\partial_t^2 + 2(\nu_s - \imath\Omega)\partial_t - (\Omega^2 - \omega_s^2 + 2\imath\nu_s\Omega)]\frac{\delta n}{n_e} = -\omega_s^2 a_1 a_2^\star \ , \qquad (28)$$

in which the inequalities $V_{g,s} \ll V_{g,1}, V_{g,2}$ have been assumed. The steady-state density perturbation predicted by the PCGO-based CBET is consequently

$$\left|\frac{\delta n}{n_e}\right| = \left|\frac{\omega_s^2 a_1 a_2^\star}{\Omega^2 - \omega_s^2 + 2\imath\nu_s\Omega}\right| \ . \qquad (29)$$

The value of this expression for the density perturbation has to be computed *a posteriori* from the global intensity field, in order to account for the contributions of all the beamlets in the $a_1 a_2^\star$ term. The resulting density perturbation map is compared to the results from HARMONY in Fig. 8. In the main resonance region (where $V > 0$, $y = 860\lambda_L$), the average and maximum values of the perturbations are both in good agreement between the PCGO-based modeling results and the HARMONY results, with $(\delta n/n_e)_{\rm mean} \simeq 5 \times 10^{-3}$ and $(\delta n/n_e)_{\rm max} \simeq 1 \times 10^{-2}$, respectively. It is not surprising to see that the IAWs amplitude in the downward velocity quadrant is slightly underestimated in the PCGO modeling, because the $V < 0$ resonance region covered by the PCGO beamlets is underestimated. Finally, we note

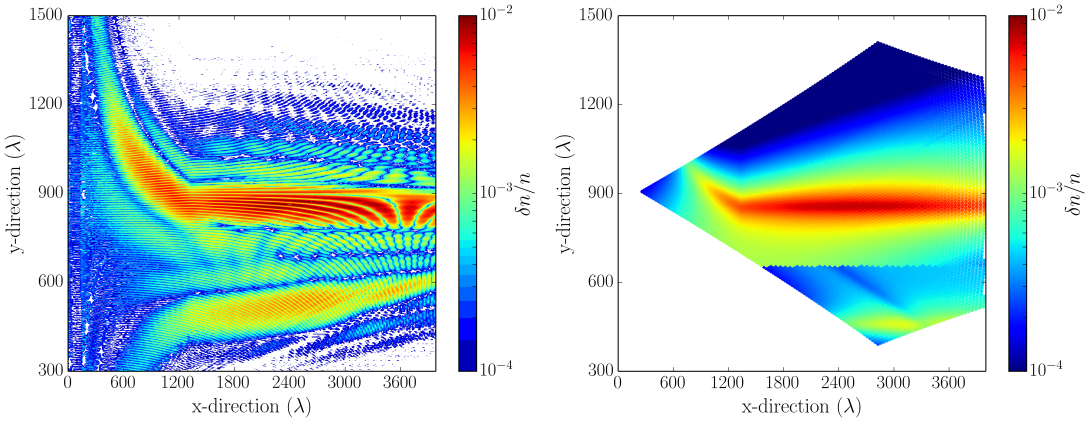

Figure 8. (color) Amplitude of the density perturbations $\delta n/n_e$ from HARMONY (left) and from PCGO (right). The simulations results correspond to the parameters $\mathcal{I}_{2:1} = 1/1$ and $[I\lambda_L^2]^\Sigma = 0.45 \times 10^{14}$ Wμm^2/cm^2.

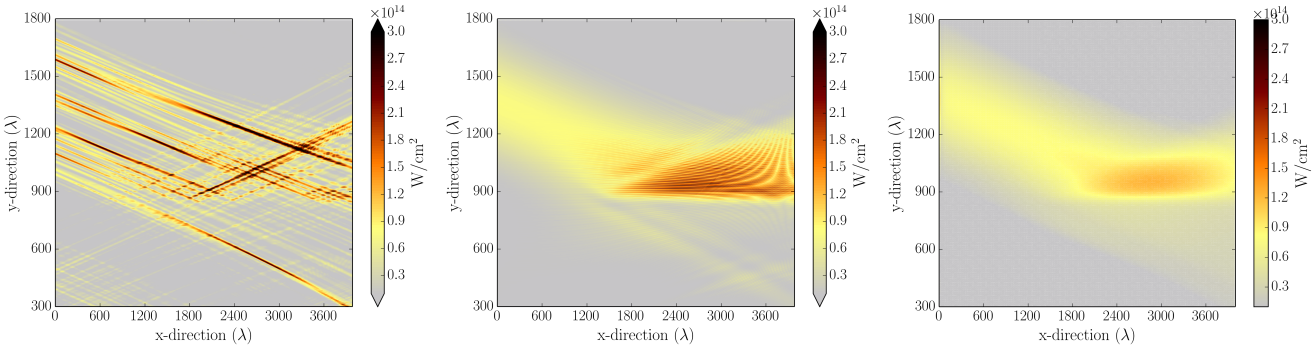

Figure 9. (color) Snapshots of the intensity pattern in the region where both beams overlap, for $\mathcal{I}_{2:1} = 1/8$ and $[I\lambda_L^2]^\Sigma = 0.9 \times 10^{14}$ Wμm^2/cm^2. The input intensity profiles correspond to RPP-smoothed smooth beams in the left panel, and to flat-top beams (so-called 'regular' beams) in the middle and the right panels, respectively. The results are from HARMONY (left, middle), and from the PCGO-based CBET model (right). The colorbar shows the corresponding values in units of 10^{14} W/cm^2 for $\lambda_L = 1$ μm. Note that some speckles in the left panel exceed the average intensity by up to 7 times (saturated colorbar).

that the spatial locations of maximum IAW amplitudes for both models are in agreement with the theoretical values of $y_{c_s,+}$ and $y_{c_s,-}$.

The spatial beam intensity patterns inside the CBET region are now compared. We inspect the beam patterns for smoothed beams with speckles (from RPP realizations) on the one hand, and the beam patterns corresponding to the 'regular' beams having the same average intensity, power, and size, but without speckles, on the other hand. In the transfer region, the RPP smoothed beams (Fig. 9 [left]), exhibit the same features in the intensity patterns (Fig. 9 [middle]) than the features observed with the regular beam, except for the fine structure of the speckles for which the intensity is several times the average intensity. Figure 9 [right] illustrates the intensity field obtained with PCGO in the case of regular beams. The domains where the pump beam is depleted and where the probe beam is preferentially amplified clearly cover the same part of the beams, in both simulations. The small-scale structure seen inside the interaction region in Fig. 9 [middle] results from the spatial and temporal interference of the beams; this small-scale structure is not reproduced by PCGO, which, by design, only can model constructive spatial interferences between beamlets. However, the average intensity value in this region is well reproduced by the PCGO model. The intensity profiles of the beams exiting at $x = 4000\lambda_L$ are illustrated in Fig. 10 [left-middle] for both the PCGO and HARMONY simulations of regular beams, respectively. They show a good agreement one with the other, in particular for the shape of the amplified beam.

This agreement is confirmed by inspecting the angular distribution of the beams, shown in Fig. 10 [right]: it is obtained via the complex fields (a_1 and a_2 in a_+) at the exit and at the entrance of the interaction zone. The angular distribution at the laser entrance at $x = 0$ for PCGO (red for the probe and blue for the pump) and for HARMONY (black), respectively, are (except for minor details) defined to be identical, corresponding to

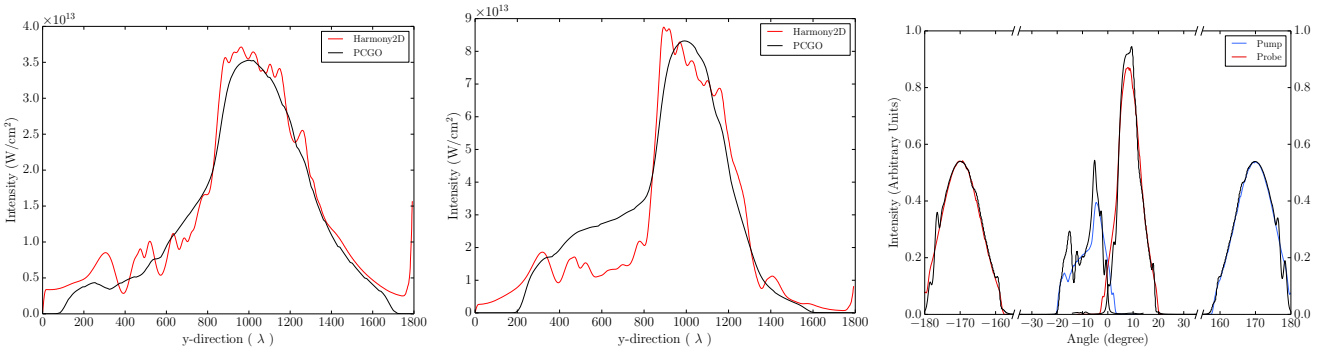

Figure 10. (color) Intensity profiles in the beam overlap region, taken at $x = 4000\lambda_L$, for $\{\mathcal{I}_{2:1} = 1,\ [I\lambda_L^2]^{\Sigma} = 0.45\}$ (left), and for $\{\mathcal{I}_{2:1} = 1/8,\ [I\lambda_L^2]^{\Sigma} = 0.9 \times 10^{14}\ \mathrm{W}\mu\mathrm{m}^2/\mathrm{cm}^2\}$ (middle). The results from HARMONY are shown in red (grey), and the results from the PCGO-based CBET model with regular beams are displayed in black. Right: intensity profiles of the beams upstream and downstream of the transfer region, as a function of the angle with the x axis. The input beams are centered at $-170°$ and $+170°$ and the output beams are centered at $-10°$ and $+10°$. The results from HARMONY are shown with black lines and the results from PCGO are displayed with colored lines. The blue (light grey) and red (dark grey) curves correspond to the pump and the probe beams, respectively. The results from HARMONY are taken past the initial transient period.

angles $\pm[160°, 180°]$. At the exit, for angles in the interval $[-30°, 30°]$, the distribution shows the same features: namely an increase and a narrowing of the peak of the probe beam, i. e. for angles in the $[0°, 20°]$ interval, and a spreading of the pump beam, i. e. for angles in $[-20°, 0°]$ interval, a beam deviation and a displacement of the barycenter of its energy density, due to the energy beam depletion.

The good agreement observed between HARMONY and the PCGO-based CBET model, in both the global energy transfer, the spatial intensity distribution and the angular distributions, provides a strong argument that the PCGO-based model can be used to compute the CBET. The advantage of the PCGO-based CBET approach lies in the computation time of each iteration, which is in the order of 10 s. In contrast, the computation with the paraxial approach requires several hours (namely 5 h on a single node of a recent processor) to achieve an asymptotic value of the power transfer after a transient period of about 30 ps; the CPU time ratio is hence in the order of 10^3. Since the CBET computation is in both cases implemented in hydrodynamic codes, in practice, one has to compare the times required to advance an interaction code over one time step of the hydro-code. For the PCGO-CBET approach, the interaction code yields its result within a time close to the time-step of the hydro-code, consequently not significantly slowing down the hydro-code computing, whereas a paraxial approach would need minutes to advance because the EM wave solver requires a smaller time step than the hydrodynamic time step.

V. EXPERIMENTAL VALIDATION OF THE CBET MODEL

We now consider the results of experimental measurements of macroscopic Crossed-Beam Energy Transfer in the case of laser beams crossing in a weakly inhomogeneous plasma. These experiments have been carried out on the NOVA laser facility[20]. A spherical polyamide shell of 1.3 mm radius containing 1 atm of C_5H_{12} gas is heated by eight laser beams of wavelength $\lambda_L = 351$ nm with a 1 ns temporal square pulse. Two additional beams intersect one to the other with the angle $\theta = 53°$, in a plasma domain close to the plasma center. The frequency of the probe pulse is varied between shots, so as to explore the resonant exchange of energy between the probe and the pump beams. The probe pulse starts at the same time as the heater beams and lasts for 2 ns, whereas the pump pulse starts 400 ps after the heater beams and lasts for 1 ns. The pump beam average intensity is $\langle I_\mathrm{p}\rangle = 10^{15}$ W/cm^2 while the probe beam intensity is varied from $0.06\langle I_\mathrm{p}\rangle$ to $0.32\langle I_\mathrm{p}\rangle$, with a wavelength shift, denoted as $\Delta\lambda$, which could be as large as 7.3 Å. The probe beam amplification $\mathcal{A}$ is defined as the probe beam transmitted energy divided by the same quantity obtained in a shot without the pump beam. Simulations of this experiment are conducted using the CHIC hydrocode[13] with the PCGO model describing the laser-plasma interaction including the propagation, absorption, and the crossed beam energy transfer.

For the 1 ns during which the interacting beams are on, the CHIC simulation predicts a relatively constant plasma density ($\sim n_e/n_c = 0.1$) in the interaction region, with an electron temperature T_e varying between 1 and 2.5 keV. The plasma expansion is rather symmetric and the velocities of the plasma flows in the interaction region are in the order of $0.01C_s$. Such low values can be explained by the symmetry of the irradiation geometry, the close proximity (400 μm) of the interaction region to the center of the target, and the early timing of the pump beam compared to the beginning of the plasma expansion. The probe-beam transfer without the pump beams is in the order of $\sim 50\%$, similarly to the results presented in Ref.

20.

The only free parameter in the PCGO-based CBET model is the damping coefficient ν_s/ω_s. According to Ref. 36, the damping rate in CH plasmas depends on the parameters $\mu \equiv k_s\lambda_D$ and $\tau \equiv T_i/T_e$. The hydrodynamic simulations show that these parameters in the interaction region vary from 0.13 to 0.235 and from 0.145 to 0.58, respectively. We resolved numerically the kinetic dispersion relation given in Ref. 36 for a C_5H_{12} plasma in this range of parameters. An additional margin of 30% was added to this range, in order to account for a potential spatial dispersion of $[\mu, \tau]$ in the vicinity of the interaction region. Among the two possible ion modes, we only consider here the slow mode which has the smaller damping. While being weakly dependent on $k_s\lambda_D$ in the relevant interval $0.1 \leq k_s\lambda_D < 0.3$, the ratio ν_s/ω_s varies from $\nu_s/\omega_s = 0.31$ to 0.17 for a T_i/T_e increase from 0.1 to 0.8. The damping rate can be fitted by the polynomial interpolation $\nu_s/\omega_s = 0.31 + 0.038\mu + 0.85\tau - 0.23\mu\tau - 0.16\mu^2 - 9.69\tau^2 + 0.25\mu\tau^2 + 0.26\tau\mu^2 + 30.12\tau^3 - 44.26\tau^4 + 31.98\tau^5 - 9.17\tau^6$ with a 0.2% accuracy. This expression is used for the inline PCGO-CBET computation.

The simulation results carried out with the PCGO-based CBET model in CHIC are compared to the experimental data in Fig. 11. Far from the domain of resonance, the probe beam amplification is rather well reproduced by the model. The energy transfer for a vanishing wavelength shift, $\Delta\lambda = 0$, is low in the simulations, as expected in view of the smallness of the plasma flows in the interaction region. The corresponding experimental probe amplification for this vanishing wavelength shift is slightly higher than what is observed in the simulations; this difference may indicate that the plasma flows are underestimated in our simulations, although the extent of the error bar for this single measurement does not allow to conclude firmly along this interpretation.

The energy transfer for a wavelength shift $\Delta\lambda > 0.55$ nm is also well reproduced within the error bars. The simulations carried out with a wavelength shift in the range $\Delta\lambda \in [0.3 : 0.52]$ nm yield a larger probe amplification than what is observed in the experimental data. The PCGO-based CBET model predicts CBET linear gains of the order of 1-1.3, while the maximum experimental gain is of the order of 1. Thus, the order of magnitude is correct, even though the experimental gains are slightly overestimated by theory. These results represent a significant improvement over other predictions of the linear gains for this experiment, of the order of ~ 20 in Ref. 20, of ~ 7 in Ref. 4, and of the order of $\sim$3-4 in the unpublished Ref. [17] of 20. The numerical results obtained from the non-paraxial code KOLIBRI[37,38] with a gain $\sim$1-1.3, such as presented in Ref. 39, are also consistent with the experimental results. The over-estimate of the energy transfer gains may simply indicate the presence of backscattering in the experiment, the latter reducing the local laser intensity in the interaction region.

The most important discrepancy between the experimental results and the theoretical predictions is found

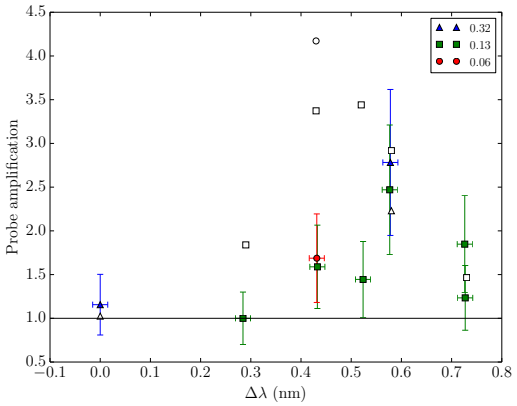

Figure 11. (color) Probe amplifications as a function of wavelength detuning, for various probe to pump intensity ratios of $\mathcal{I}_\mathcal{I} = 0.32$ (triangles), 0.13 (squares) and 0.06 (circles). The probe beam transmission being reproducible to $\pm 15\%$[20]. The error in the energy ratio between experiments is estimated at $\pm 30\%$. Simulation results are superimposed as empty symbols.

in the position of the resonance peak in λ-space, located around $\Delta\lambda_{\rm sim}^{\rm peak} \sim 0.48$ nm (for $\mathcal{I}_{2:1} = 0.13$) in the simulations and $\Delta\lambda_{\rm exp}^{\rm peak} \sim 0.6$ nm (for $\mathcal{I}_{2:1} = 0.13$) in the experiment. This discrepancy is discussed in the following, together with the resonance width.

The experimental results are analyzed in the framework described in Sec. II. In order to analyze the dependence of the results shown in Fig. 11 with regards to the wavelength shift $\Delta\lambda$, we make the following assumptions: the plasma parameters are (i) constant across the interaction region, (ii) constant during the interaction time, (iii) constant for shots with different values of $\Delta\lambda$, (iv) constant for shots without the pump beam, and, (v), we assume that the lasers upstream intensity is stable from shot to shot. The probe beam amplification factor $\mathcal{A}$ can consequently be assimilated to the amplification factor $\exp(G)$, G being the linear gain factor. The dependence of G on the wavelength detuning between the laser beams can be estimated from Eqs. (9) and (13):

$$G(\Delta\lambda) \propto G_0 \left(1 + \left[\frac{\omega_p}{(\nu_s(1 + \lambda_p/(\Delta\lambda - \Delta\lambda^{\rm peak}))}\right]^2\right)^{-1}, \tag{30}$$

where G_0 is the maximum gain obtained at resonance for $\Delta\lambda = \Delta\lambda^{\rm peak}$. A nonlinear least-square fit of the gain function defined above can be made with the experimental data and the simulation results (for $\mathcal{I}_{2:1} = 0.13$). Although this approach is only qualitative, it makes it possible to estimate the temporally- and spatially-averaged damping rate $\bar{\nu_s}$ in the experiment, and to discuss the position of the resonance. As illustrated in Fig. 12, the averaged damping rates (i.e. the width of the resonance function) are similar in the simulations and in the experiments, with $\bar{\nu_s}^{\rm exp} = 1.93$ ps^{-1} and $\bar{\nu_s}^{\rm sim} = 2.67$ ps^{-1}.

Accounting for the temporal and spatial variations of the sound speed and of ν_s/ω_s in the interaction region and during the duration of the interaction, the damping rate found in the simulations, namely $\nu_s \in [0.97, 5.3]$ ps^{-1}, brackets the value estimated from the gain curves.

The difference of the positions in λ-space of the resonance peaks observed in the experiments and in the simulations is 1.2 Å. This resonance peak position uniquely depends on the Doppler shift, which in turn is a function of the local sound speed velocity and of the irradiation symmetry. We now consider the various contributions which may explain the observed difference in the resonance peak positions. Several simulations were conducted using the ideal gas law instead of the SESAME Equation of States (see Fig. 12), without any significant difference in the sound velocity. If one assumes that the plasma flow is aligned along $\mathbf{k}_s$, the plasma velocity required to shift the resonance by 1.2 Å is of the order of$\sim 0.25c_s$. The hydrodynamic simulations predict that the velocity vector is directed outward from the center of target, so that $\phi \sim 98°$. With such an angle, the plasma flow velocity needed to Doppler shift the resonance by the amount mentioned just above would be $\sim 1.2c_s$, a significant and unlikely value for the central region of a gas bag target. This conclusion indicates that if the resonance is shifted due to the plasma expansion, it arises from hydrodynamic asymmetries which turn the velocity vector in the k_s direction. In view of the the probe beam angle and intensity, a strong ponderomotive force could shift the velocity vector in the right direction. However, the simulations using the ponderomotive force module based on PCGO[14] suggest that this effect is not relevant here: the added ponderomotive pressure is not strong enough to rotate the local velocity vector significantly.

Another tentative explanation of the resonance shift is related to the effect of the laser spectral width on the energy transfer. Simulations conducted for spectrally broadened interaction beams with $\Delta\lambda_{\text{spread}} = 2.5$ Å have shown that the simulated resonance peak is displaced toward the value observed in the experiment by +0.25 Å, as shown in Fig. 12. However, the resonance width also appears larger, which tempers the relevance of this assumption.

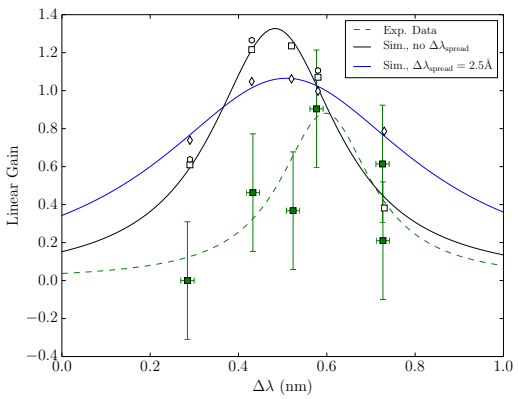

Figure 12. (color) Linear gain curves as a function of the wavelength detuning between the beams. The simulation results are presented as black open symbols and the experimental data points as green squares. Concerning the simulations, the squares indicate the results obtained with the SESAME EOS, and the circles those obtained with the ideal gas law. The diamonds correspond to simulation results with a laser spectral width of $\Delta\lambda_{\text{spread}} = 2.5$ Å. The corresponding fits to a Lorentzian gain function are presented as solid lines.

VI. CONCLUSION

The modeling of the macroscopic Crossed-Beam Energy Transfer between Gaussian optical beamlets, such as described by Paraxial Complex Geometrical Optics, has been compared to (i) theoretical formulations of the CBET gains in the case of laser beams propagating in an inhomogeneous plasma, (ii) a time-dependent paraxial description coupled to a nonlinear fluid model with the code HARMONY, and (iii) measurements, in a gas-bag experiment, of the CBET gain as a function of the wavelength detuning between the crossing beams.

The PCGO-based CBET approach is shown to reproduce the linear gains and the beam deviation angles such as given by the theory of a steady-state energy transfer in an inhomogeneous plasma. A comparison to the time-dependent paraxial simulations with the code HARMONY confirms that the PCGO-based approach is able to reproduce correctly the linear gains on a large range of parameters $\mathcal{I}_{2:1}$ and $I\lambda_L^2$, past a transient phase and in the conditions where a steady-state regime exists. In the latter cases, it is seen that the PCGO-based model (i) reproduces the correct spatial repartition of the intensity field inside the CBET region and provides a correct estimate of the beams deviations, and (ii) can be used to estimate the location and the values of the amplitudes of the IAWs excited interacting beams. In the cases where a steady-state does not exist, the PCGO-based model yields estimates of the linear CBET gain that is close to the reference solution. The non-stationary situations reported here are caused by the presence of two resonance regions in the interaction volume with opposite energy transfer directions. The speckle structure of the crossing smoothed laser beams appears to play a role when the number of speckles inside the crossing volume is small. This case is more likely to occur for larger f-numbers as compared to our study, and it might eventually lead to an increasing error in the successive crossed beam interactions.

Finally, a good agreement with a reference experiment for CBET was found, with linear gains close to the measured ones, although slightly overestimated. This agreement is significantly better than the previous estimates made for this experiment. The model predicts optimal wavelength detuning for the energy exchange slightly different than what is observed in the experiment. It is

unlikely that this discrepancy originates from a Doppler shift effect, unless significant velocity asymmetries were present in every shot. If one assumes that the linear gains given by the PCGO-based model are overestimated, accounting for the spectral width of the laser light gives a gain function which could agree with all of the experimental error-bars. Thus, the maximum gain detuning observed in the experiment could be explained by statistical fluctuations of the laser and plasma parameters.

These comparisons provide a solid validation of the PCGO-based approach as a mean to model CBET at hydrodynamic scales. It is sufficiently fast to be coupled to a large scale radiative hydrodynamic code, which is of great interest for the modeling of CBET in ICF and the design of high intensity laser-target experiments involving overlapping beams.

VII. ACKNOWLEDGMENTS

This work has been carried out within the framework of the EUROfusion Consortium and has received funding from the Euratom research and training programme 2014-2018 under grant agreement No 633053. The views and opinions expressed herein do not necessarily reflect those of the European Commission. This work has been partially supported by the *Agence Nationale de Recherche*, project title "Ilphygerie" no. ANR-12-BS04-0006.

REFERENCES

[1]K. Tanaka, L. M. Goldman, W. Seka, M. C. Richardson, J. M. Soures, and E. A. Williams, Phys. Rev. Lett. **48**, 1179 (1982).
[2]W. Seka, E. A. Williams, R. S. Craxton, L. M. Goldman, R. W. Short, and K. Tanaka, Phys. Fluids **27**, 2181 (1984).
[3]T. Afshar-rad, L. A. Gizzi, M. Desselberger, F. Khattak, O. Willi, and A. Giulietti, Phys. Rev. Lett. **68**, 942 (1992).
[4]W. L. Kruer, S. C. Wilks, B. B. Afeyan, and R. K. Kirkwood, Phys. Plasmas **3**, 382 (1996).
[5]S. W. Haan, S. M. Pollaine, J. D. Lindl, L. J. Suter, R. L. Berger, L. V. Powers, W. E. Alley, P. A. Amendt, J. A. Futterman, W. K. Levedahl, M. D. Rosen, D. P. Rowley, R. A. Sacks, A. I. Shestakov, G. L. Strobel, M. Tabak, S. V. Weber, G. B. Zimmerman, W. J. Krauser, D. C. Wilson, S. V. Coggeshall, D. B. Harris, N. M. Hoffman, and B. H. Wilde, Phys. Plasmas **2**, 2480 (1995).
[6]P. Michel, L. Divol, E. A. Williams, S. Weber, C. A. Thomas, D. A. Callahan, S. W. Haan, J. D. Salmonson, S. Dixit, D. E. Hinkel, M. J. Edwards, B. J. MacGowan, J. D. Lindl, S. H. Glenzer, and L. J. Suter, Phys. Rev. Lett. **102**, 025004 (2009).
[7]I. V. Igumenshchev, D. H. Edgell, V. N. Goncharov, J. A. Delettrez, A. V. Maximov, J. F. Myatt, W. Seka, A. Shvydky, S. Skupsky, and C. Stoeckl, Phys. Plasmas **17**, 122708(5) (2010).
[8]I. V. Igumenshchev, W. Seka, D. H. Edgell, D. T. Michel, D. H. Froula, V. N. Goncharov, R. S. Craxton, L. Divol, R. Epstein, R. Follett, J. H. Kelly, T. Z. Kosc, A. V. Maximov, R. L. McCrory, D. D. Meyerhofer, P. Michel, J. F. Myatt, T. C. Sangster, A. Shvydky, S. Skupsky, and C. Stoeckl, Phys. Plasmas **19**, 056314(12) (2012).
[9]T. B. Kaiser, Physical Review E **61**, 895 (2000).
[10]P. Michel, S. H. Glenzer, L. Divol, D. K. Bradley, D. Callahan, S. Dixit, S. Glenn, D. Hinkel, R. K. Kirkwood, J. L. Kline, W. L. Kruer, G. A. Kyrala, S. Le Pape, N. B. Meezan, R. Town, K. Widmann, E. A. Williams, B. J. MacGowan, J. Lindl, and L. J. Suter, Phys. Plasmas **17**, 056305 (2010).
[11]Y. A. Kravtsov, Radiophysics and Quantum Electronic **10(9-10)**, 719 (1967).
[12]Y. A. Kravtsov and P. Berczynski, Studia Geophysica et Geodaetica **51** (2007).
[13]J. Breil, S. Galera, and P. H. Maire, Computers & Fluids **46**, 161 (2011).
[14]A. Colaïtis, G. Duchateau, P. Nicolaï, and V. Tikhonchuk, Phys. Rev. E **89**, 033101 (2014).
[15]A. Colaïtis, G. Duchateau, X. Ribeyre, and V. Tikhonchuk, Phys. Rev. E **91**, 013102 (2015).
[16]C. J. McKinstrie, A. V. Kanaev, V. T. Tikhonchuk, R. E. Giacone, and H. X. Vu, Phys. Plasmas **5**, 1142 (1998).
[17]D. Pesme, S. Hüller, J. Myatt, C. Riconda, A. Maximov, V. T. Tikhonchuk, C. Labaune, J. Fuchs, S. Depierreux, and H. A. Baldis, Plasma Physics and Controlled Fusion **44**, B53 (2002).
[18]S. Hüller, P. E. Masson-Laborde, D. Pesme, M. Casanova, F. Detering, and A. Maximov, Phys. Plasmas **13**, 022703 (2006).
[19]P. E. Masson-Laborde, S. Hüller, D. Pesme, C. Labaune, S. Depierreux, P. Loiseau, and H. Bandulet, Phys. Plasmas **21**, 032703 (2014).
[20]R. K. Kirkwood, B. B. Afeyan, W. L. Kruer, B. J. MacGowan, J. D. Moody, D. S. Montgomery, D. M. Pennington, T. L. Weiland, and S. C. Wilks, Phys. Rev. Lett. **76**, 2065 (1996).
[21]D. Pesme, "in *La fusion thermonucléaire inertielle par laser: l'interaction laser-matière part. 1*," (Eyrolles, Paris, 1993) pp. 373, 494–495.
[22]C. J. McKinstrie, J. S. Li, R. E. Giacone, and H. X. Vu, Phys. Plasmas **3**, 2686 (1996).
[23]M. N. Rosenbluth, Phys. Rev. Lett. **29**, 565 (1972).
[24]Y. A. Kravtsov and N. Y. Zhu, Theory of Diffraction, Heuristic Approaches, Alpha Science Series on Wave Phenomena (Alpha Science International LTD., Oxford, U.K., 2010).
[25]P. N. Brown, A. C. Hindmarsh, and L. R. Petzold, SIAM Journal on Scientific Computing **15**, 1467 (1994).
[26]P. N. Brown, A. C. Hindmarsh, and L. R. Petzold, SIAM Journal on Scientific Computing **19**, 1495 (1998).
[27]A. Hindmarsh and A. Taylor, "User documentation for IDA: A differential-algebraic equation solver for sequential and parallel computers," Lawrence Livermore National Laboratory report, UCRL-MA-136910 (1999).
[28]H. A. Rose and D. F. DuBois, Phys. Fluids B **5**, 590 (1993).
[29]J. Garnier, Physics of Plasmas **6**, 1601 (1999).
[30]S. Hüller and A. Porzio, Laser and Particle Beams **28**, 463 (2010).
[31]T. Speziale, Phys. Fluids **27**, 2583 (1984).
[32]M. Maier, W. Kaiser, and J. A. Giordmaine, Phys. Rev. **177**, 580 (1969).
[33]C. J. Randall, J. R. Albritton, and J. J. Thomson, Physics of Fluids **24**, 1474 (1981).
[34]S. Hüller, P. Mulser, and A. M. Rubenchik, Physics of Fluids B **3**, 3339 (1991).
[35]J. F. Myatt, J. Zhang, R. W. Short, A. V. Maximov, W. Seka, D. H. Froula, D. H. Edgell, D. T. Michel, I. V. Igumenshchev, D. E. Hinkel, P. Michel, and J. D. Moody, Phys. Plasmas **21**, 055501 (2014).
[36]E. A. Williams, R. L. Berger, R. P. Drake, A. M. Rubenchik, B. S. Bauer, D. D. Meyerhofer, A. C. Gaeris, and T. W. Johnston, Phys. Plasmas **2**, 129 (1995).
[37]S. Hüller, P. Mounaix, and D. Pesme, Physica Scripta **T63**, 151 (1996).
[38]S. Hüller, P. Mounaix, V. T. Tikhonchuk, and D. Pesme, Physics of Plasmas **4**, 2670 (1997).
[39]P. Loiseau, Crossed beam energy transfer in the context of a MegaJoule laser Ph.D. thesis, (in French), Université Paris XI (1999).